



*Citation for published version:*

Amitrano, D, Cecinati, F, Martino, GD, Iodice, A, Mathieu, PP, Riccio, D & Ruello, G 2018, 'Feature Extraction From Multitemporal SAR Images Using Selforganizing Map Clustering and Object-Based Image Analysis', IEEE Journal of Selected Topics in Applied Earth Observations and Remote Sensing, vol. 11, no. 5, pp. 1556 - 1570. <https://doi.org/10.1109/JSTARS.2018.2808447>

*DOI:*

[10.1109/JSTARS.2018.2808447](https://doi.org/10.1109/JSTARS.2018.2808447)

*Publication date:*

2018

*Document Version*

Peer reviewed version

[Link to publication](#)

*Publisher Rights*

Unspecified

(c) 2018 IEEE. Personal use of this material is permitted. Permission from IEEE must be obtained for all other users, including reprinting/ republishing this material for advertising or promotional purposes, creating new collective works for resale or redistribution to servers or lists, or reuse of any copyrighted components of this work in other works.

## University of Bath

**General rights**

Copyright and moral rights for the publications made accessible in the public portal are retained by the authors and/or other copyright owners and it is a condition of accessing publications that users recognise and abide by the legal requirements associated with these rights.

**Take down policy**

If you believe that this document breaches copyright please contact us providing details, and we will remove access to the work immediately and investigate your claim.

# Feature extraction from multitemporal SAR images using self-organizing map clustering and object-based image analysis

Donato Amitrano, Francesca Cecinati, Gerardo Di Martino, *Senior Member, IEEE*, Antonio Iodice, *Senior Member, IEEE*, Pierre-Philippe Mathieu, Daniele Riccio, *Fellow, IEEE*, Giuseppe Ruello, *Member, IEEE*

**Abstract**—We introduce a new architecture for feature extraction from multitemporal synthetic aperture radar data. Its purpose is to combine classic synthetic aperture radar processing and geographical object-based image analysis to provide a robust unsupervised tool for information extraction from time series images. The architecture takes advantage from the characteristics of the recently introduced RGB products of the Level-1 $\alpha$  and Level-1 $\beta$  families, and employs self-organizing map clustering and object-based image analysis. In particular, the input products are clustered using color homogeneity and automatically enriched with a semantic attribute referring to clusters' color, providing a pre-classification mask. Then, in the frame of an application-oriented object-based image analysis, opportune layers measuring scattering and geometric properties of candidate objects are evaluated, and an appropriate rule-set is implemented in a fuzzy system to extract the feature of interest. The obtained results have been compared with those given by existing techniques and turned out to provide high degree of accuracy and negligible false alarms. The discussion is supported by an example concerning small reservoir mapping in semi-arid environment.

**Index Terms**—self-organizing maps, synthetic aperture radar, object-based image analysis, multitemporal, classification

## I. INTRODUCTION

Earth observation exploitation in operational/industrial contexts is today still limited, because it requires to end-users, who are mainly used to work in geographical information system (GIS) environments, to handle sophisticated data analysis algorithms. This is especially true for synthetic aperture radar (SAR) data, which are largely underused due to the high expertise required to handle/interpret them. Therefore, the development of new tools for complex satellite data management, integrating remote sensing and GIS technologies, is desirable for enlarging the user community.

To this aim, many authors suggest to balance perceptive insights and mathematics for building end-user-oriented/multidisciplinary processing chains [1]–[5]. Research on these topics lead to a huge literature on knowledge-driven expert systems [6]–[8] constituting the basis of modern geographical object-based image analysis (GEOBIA) [9], whose

classic schema is summarized by the flowchart depicted in Fig. 1b. This approach aims at extracting information from remote sensing data by mimicking the way in which humans visually interpret images [10], [11], analyzing spectral information (e.g. colors), spatial characteristics (e.g. size, shape), textural, and contextual information (e.g. relation with neighboring objects) [12].

The crucial step for applying object-based techniques to remote sensing images is the object definition. This is typically done through segmentation, obtaining good results with optical data. This approach can not be applied to SAR images as is, because the speckle reduces the segmentation performances and the extraction of the semantics from the image is not immediate. Accordingly, at the state of the art, common practice in SAR data processing is still to focus the innovation on algorithms [13]–[17], following the scheme reported in Fig. 1a.

In this paper, we devise a novel architecture for feature extraction based on innovative SAR remote sensing processing allowing for the extension of GEOBIA techniques to SAR time series. The goal is the creation of a bridge between GEOBIA and SAR communities, providing easy-to-use tools for data exploitation. The proposed architecture takes advantage of consolidated techniques, as self-organizing map clustering (SOM) [18] and object-based image analysis (OBIA) [19], and exploits the characteristics of the innovative multitemporal SAR data processing introduced by the authors [5], [20], as synthesized in Fig. 1c.

In particular, we exploit the recently introduced products of the Level-1 $\alpha$  and Level-1 $\beta$  families [5], [20]. They are semi-finished products obtained from SAR time series opportunely combined in a RGB frame. A multitemporal Level-1 $\alpha$  or Level-1 $\beta$  image is treated with a clustering algorithm to obtain meaningful regions (see the fourth block of Fig. 1c), each of them associated to a basic verbal attribute related to its color. This algorithm is derived from Kohonen's SOM clustering [18] and tailored on the characteristics of the input products, exploiting color homogeneity as discriminant for pixel aggregation. The clustered map, enriched by the basic semantic attribute, is processed with an application-oriented OBIA (fifth block of Fig. 1c). In fact, the color label is used to build a pre-classification mask, whose objects are analyzed with an opportune rule set allowing for the extraction of the feature of interest. The proposed approach provides a minimization of the number of free parameters, which is one of the biggest

Donato Amitrano, Gerardo Di Martino, Antonio Iodice, Daniele Riccio, and Giuseppe Ruello are with the Department of Electrical Engineering and Information Technology, University of Napoli Federico II, Napoli, Italy {email: donato.amitrano@unina.it, gerardo.dimartino@unina.it, iodice@unina.it, dariccio@unina.it, ruello@unina.it}.

Francesca Cecinati is with the University of Bath, Bath, UK {email: f.cecinati@bath.ac.uk}.

Pierre-Philippe Mathieu is with the European Space Agency, ESA ESRIN, Frascati, Italy {email: Pierre.Philippe.Mathieu@esa.int}.

problems in GEOBIA [21].

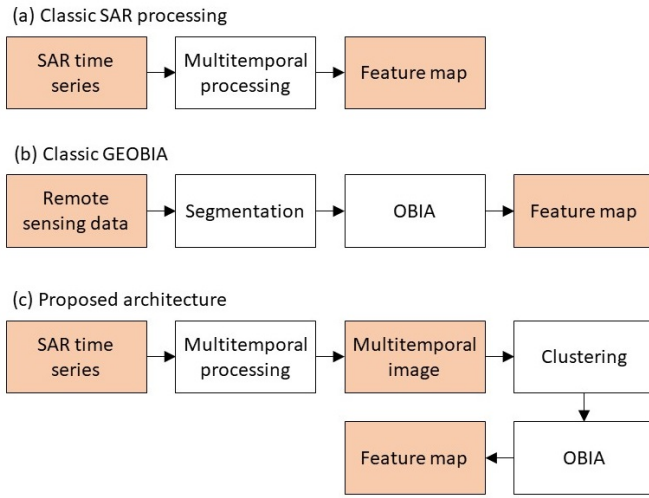


Fig. 1: (a) Classic SAR processing, (b) classic GEOBIA, and (c) proposed architecture. Boxes with filled background represent products. Those with blank background identify processes.

The organization of the paper recalls the flowchart of Fig. 1c. The first three blocks have been deeply addressed in [5], [20], and [22], and will be only recalled all over the paper, where necessary. The modified SOM algorithm is presented in Section II. The proposed OBIA technique is discussed in an application-oriented environment in Section III, where we address the problem of small reservoir mapping in semi-arid environment. Conclusions are drawn at the end of the work.

## II. MODIFIED SOM CLUSTERING

SOM, is a machine-learning technique of the artificial neural network (ANN) family. It has been exploited to classify the most diverse data types in different sectors, from climatology [23] to political science [24], finance [25], and remote sensing [26]. This widespread use of SOM is due to its high flexibility and adaptability. In fact, a ANN do not make assumptions on the statistical distribution of the data, and this makes it possible its application to heterogeneous datasets and modification/integration for adaptation to different data structures [27] and learning techniques [28]. The robustness to large amounts of data make ANNs a suitable instrument for unsupervised or semi-supervised classification in a big-data environment, which is, and will be a crucial issue in remote sensing.

The SOM principle is schematized in Fig. 2, in which nodes are constituted by RGB triplets. The number of (pre-defined) nodes (or neurons), having the same structure of the data to be classified, will coincide with the number of output classes. In the classic Kohonen's schema, these nodes are randomly initialized (Fig. 2a) and connected by a (usually) rectangular structure. They are trained using a pre-defined number of sample vectors randomly selected from the input data. Each time a training vector is presented to the network, the most similar node (i.e. the one minimizing the objective function

given by the Euclidean distance) is detected and identified as the best matching unit (BMU). The BMU and its neighbor, defined by a radius, are updated to become more similar to the presented training set, as shown in Fig. 2b. This operation is repeated for several iterations, called epochs. At the end of each epoch, the neighbor of the BMU as well as the learning rate are decreased. This way, after many epochs, the SOM becomes stable, i.e. it does not exhibit significant changes with respect to the previous epoch, and the obtained nodes can be used to classify data.

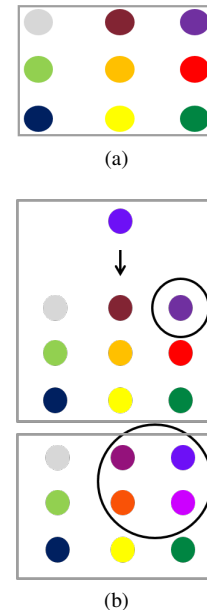


Fig. 2: SOM principle. (a) Initial, randomly initialized SOM. (b) The BMU and its neighbor are updated to become more similar to the presented training set.

As aforementioned, SOMs can be easily modified to be adapted to specific data [27], [28], and this made them very attractive for the clustering of our SAR-derived RGB products. As an example, in the initialization phase, neurons are typically randomly selected. As a consequence, the SOM output will be slightly different for different executions given the same set of network parameters. In our case, we need the output cluster map to be stable with respect to the input RGB product. To this end, we established a data-driven seed to initialize neurons and to generate the training samples. In such way, for a given RGB product, the output SOM is fixed by its parameters.

As for the training phase, we implemented the following procedure. A matrix of  $M \times 3$  RGB triplets is randomly generated using the aforementioned seed. In order to consider more combinations of the primary colors,  $M$  is greater than the pre-established number  $T$  of training vectors. These random triplets are made consistent with the re-quantization problem by computing pixel-wise the Euclidean distance between the  $i$ -th training set and the input RGB product. Finally, among the  $M$  available triplets, the  $T$  more similar to a color existing in the input RGB product are selected as training sets.

As stated in [8], one of the knowledge required for under-

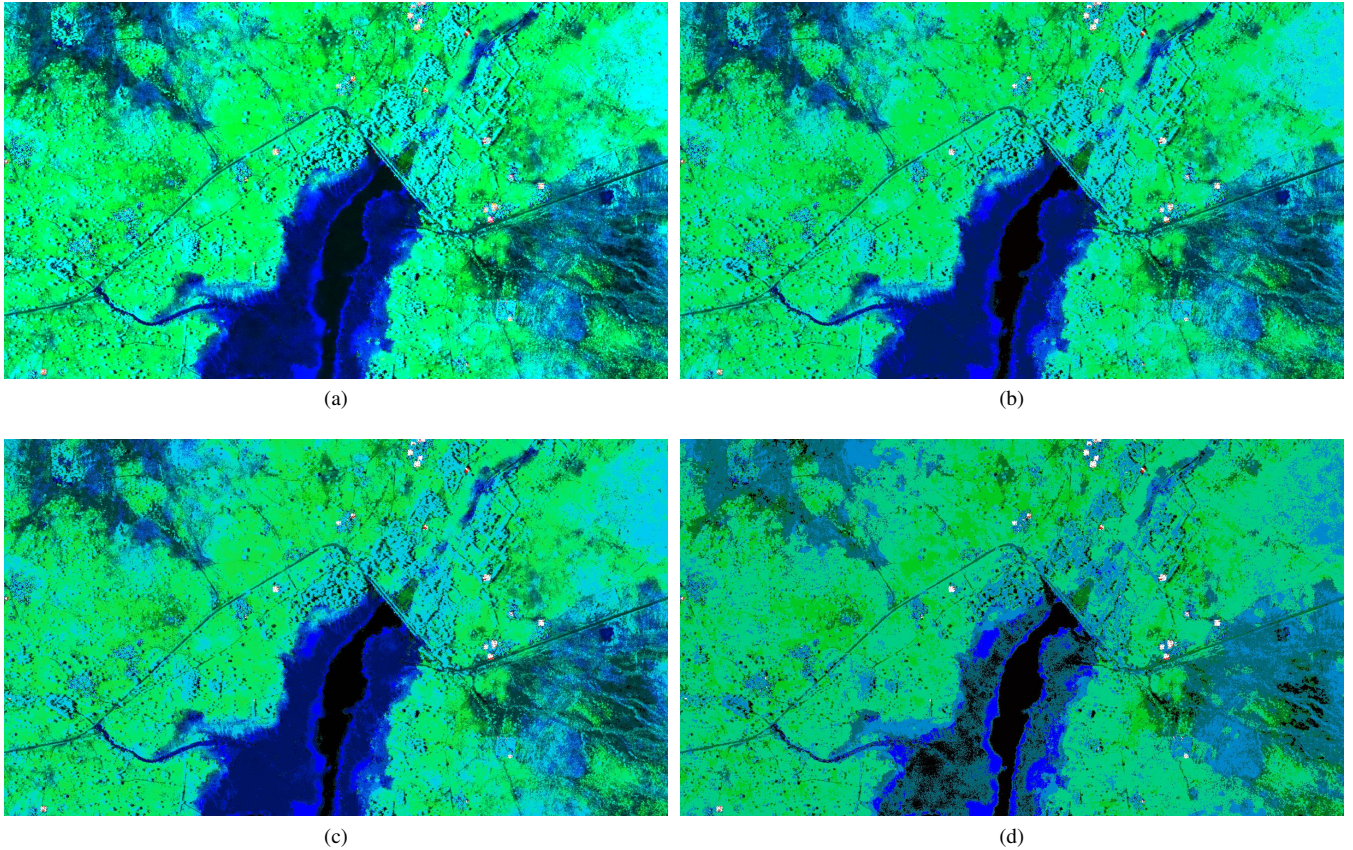


Fig. 3: Result of SSOM clustering varying the dimension of the output feature space. (a) Input RGB product. (b) 49-cluster product. (c) 25-cluster product. (d) 9-cluster product.

standing remote sensing images concerns the mapping of scene features into the image acquired by the sensor. Therefore, in order to better adapt the classic Kohonen’s scheme to the input data, we slightly modified the algorithm presented in [18].

As an example, let us consider the Level-1 $\alpha$  product depicted in Fig. 3a. It represents a rural area in Burkina Faso (Western Africa). In this region, the climate is semi-arid, with a long dry season (at the peak of which the environment is almost completely dry) followed by a short and intense wet season, in which the abundant rainfalls allow for cultivation and water and food storage [29]. In this product, the red, green, and blue bands are assigned to the interferometric coherence, to a wet season image, and to a dry season image, respectively. This composition allows for displaying in natural colors the seasonal water (in blue, due to the dominance of terrain scattering during the dry season) and the vegetation (in green, due to volumetric scattering enhancement triggered by vegetation growing during the wet season). For more information about Level-1 $\alpha$  imagery, the reader can refer to [5].

In this scene, natural land cover is dominant with respect to the “urban class”, which consists in small settlements represented by bright targets [5]. Therefore, if the classic Kohonen’s algorithm is used, very few training set belonging to this category would be presented to the network. As a result, it is likely that the “urban” cluster will be not represented

in the final SOM. To overcome this problem, we impose the presence of the white, black, and red colors among the training sets to be used in the competitive phase. In fact, these colors are associate to precise classes (such as built-up features, water surfaces and low-backscattering areas) which are likely to be present in every acquisition, even if with small occurrence with respect to other classes. Moreover, in order to ensure the presence of such colors in almost pure tonality within the final SOM, when the relevant training sets are presented to the network, it behaves as in a Learning Vector Quantization (LVQ) schema [18], in which only the winning neuron is updated with a high learning rate.

The objective of using a SOM is to map the input product from the RGB space, whose dimension is  $[256 \times 256 \times 256]$ , into a space  $\hat{S}$  with a limited number of elements (i.e. coinciding with the number of SOM neurons). At the same time, we aim at enriching the obtained cluster map with a basic semantic, i.e. to label each element of  $\hat{S}$  with a meaningful word recalling a physical property of the cluster. This makes the SOM semantic (SSOM), allowing for querying the image in the feature space exploiting the cluster label.

To this end, a HTML color database is considered for picking the cluster label. The Euclidean distance between the SOM and the database elements is computed. Finally, for each SOM cluster, the name of the closest color within the database is assigned.



Fig. 4: Sample 49-cluster SSOM referring the the image depicted in Fig. 3a. Each cluster is associated to one of the color labels enumerated on the right. The association color label-SSOM cluster is made column-wise from up to down and from left to right. Similar colors can have the same color label.

In Fig. 3, we show the output of the SSOM clustering, setting the dimension of  $\hat{S}$  (i.e. the size of the SSOM) to 49 (Fig. 3b), 25 (Fig. 3c), and 9 (Fig. 3d) elements. In Fig. 4, a sample SSOM for the 49-cluster case is reported together with the relevant color label list. In this picture, the association color label-SSOM cluster is made column-wise from up to down and from left to right. Note that very similar colors can have the same label.

From Fig. 3, it arises that the larger the number of clusters in the output product, the more similar the (pre)-classified image to the input RGB one. In fact, as shown in Fig. 3d, when the dimension of  $\hat{S}$  is reduced to 9 elements, its colorimetric content becomes insufficient to describe effectively the information contained in the input Level-1 $\alpha$  product, causing the loss of the physical relation between the colors in the clustered product and the scene objects (see as an example gray pixels in the lake area in Fig. 3d).

However, beyond interpretability, the principal purpose of clustering is to provide a product useful to be processed automatically by the machine. This means that a number of clusters appropriate for human interpretation could be not sufficient (in the sense that the image could result under-segmented) to address a certain problem using a computer algorithm. Actually, in the framework of the method outlined in Section I, the number of SSOM clusters is very important and can greatly affect the performance of the processing chain. The problem will be addressed with an empirical approach in Section III-F to face the problem of small reservoir mapping in semi-arid environment.

### III. APPLICATION-ORIENTED OBIA: SMALL RESERVOIR MAPPING IN SEMI-ARID ENVIRONMENT

The processing chain outlined in Section I is strongly application-oriented since the management of the semantics

introduced by the SSOM clustering, as well as the OBIA, need to be adapted to the feature of interest. In other words, if the general processing depicted in the last diagram of Fig. 1 can be replicated to address different problems (see as an example [30] for a preliminary experiment dealing with urban area mapping), the OBIA block has to be adapted to the scattering and geometrical characteristics of the objects one wants to identify, represented in this case by small reservoirs in semi-arid environment.

In semi-arid environment, small reservoirs constitute a fundamental resource for local population (especially in rural areas) to face water scarcity during long periods of drought [31], [32]. In Burkina Faso, that is the country in which our study area is located, it is estimated that about 1700 small reservoirs are actually used for irrigation, livestock, and human consumption. However, despite of their importance, reservoirs are rarely appropriately monitored in low-income countries, especially in Sub-Saharan Africa [32]. Moreover, small reservoirs are often built/modified by local communities without governmental coordination and even basic data, like their location and capacity, are not available. For these reasons, it is extremely hard to study their impact on the territory and to optimize their management.

Remote sensing technologies have been widely exploited to address this problem [33]–[37], which is particularly discussed in the community, also thanks to the TIGER initiative of the European Space Agency [38]. Using SAR data, small reservoirs are usually mapped using pixel-based segmentation techniques providing results characterized by good accuracy, but with an incidence of false alarm that sometimes is not negligible [36]. In this work, we want to demonstrate that the proposed methodology allows for reducing drastically the false alarm rate keeping, at the same time, the accuracy comparable to that given by the most popular SAR segmentation

algorithms.

The general flowchart of the method we are going to apply is depicted in Fig. 5. In this picture, boxes and arrows with red edges represent an exploded view of the block “OBIA” of the last graph depicted in Fig. 1. Boxes with filled background represent products. Those with blank background identify processes.

Although at first glance it could appear complicated, the flowchart is composed by a series of very simple operations dictated by the experience and regulated, when necessary, by fuzzy rules. Indeed, it is inline with the GEOBIA philosophy, whose objective is to mime the human behavior in the understanding of the surrounding environment. In fact, humans understand the world and operate in it through a series of simple operations, which become obvious with the experience. The reader can think, as an example, to the trivial operation of pouring water from a bottle into a glass for drinking. Clearly, several basic operation must be implemented, such as: segment the scene to localize the bottle and the glass, take the bottle, pour water into the glass, replace the bottle and then drink water using the glass. The concept we adopted in the design of the flowchart reported in Fig. 5 is exactly the same, i.e. the implementation of several simple operation to understand the scene up to the extraction of its reservoirs.

Roughly, the proposed processing chain is the following. The input RGB product is treated with SSOM clustering and a relevant set of words is identified to be representative of the class “small reservoirs”. Clusters associated to this class constitute a over-dimensioned pre-classification mask, identifying objects candidate to be classified as reservoirs. This mask is treated with OBIA, whose aim is to identify objects whose scattering and geometric characteristics are most likely to be those of a reservoir. To this end, two object layers are exploited. The first one is the mean (computed within each image object) of the seasonal water pseudo-probability (SWPP) [36]. It represents a scattering layer. The second one, representing a geometric layer, is the objects’ compactness [39].

In the following paragraphs, we will provide a complete description of all the aforementioned operations.

#### A. Dictionary definition

This paragraph describes the blocks indexed with 1 and 2 in Fig. 5.

The input of the processing chain is a change-detection-oriented Level-1 $\alpha$  product in which the blue band is acquired at the peak of the dry season. As explained in Section II, this causes small reservoirs to be rendered in blue color (see [5] for further details).

The input RGB product is treated with the SSOM algorithm discussed in Section II, and the associated color labels considered for the dictionary definition. This operation is guided by the knowledge of Level-1 $\alpha$  products characteristics and of their mapping into the SSOM. As a result, the following color labels were selected as the most representative of the class “small reservoir” (see Fig. 4): “Blue”, “Navy blue”, “Royal blue”, “Medium blue”, and “Midnight blue”. A non-expert

user can reach the same result empirically through visual inspection of the cluster map. Selecting a region representing a reservoir and computing the statistics, it will result that more than 90% of pixels within the area of interest belong to the above listed classes.

The idea is to build a over-dimensioned pre-classification map to be eroded through the successive OBIA steps in order to reach the final reservoirs map. An example of this operation is provided in Fig. 6. In particular, in Fig. 6a, a Level-1 $\alpha$  product concerning one of the reservoirs of the study area is shown. The corresponding 49-cluster SSOM is shown in Fig. 6b. The semantic mask obtained considering all the pixels having a color label included in the dictionary is depicted in Fig. 6c. The mixing of land and water features may cause the object to loose the characteristics of scattering (on average) and the geometric properties useful to classify it as a reservoir.

To prevent this, a suitable management of the dictionary is necessary. In particular, it is split in a “reliable” part and in a “unreliable” part. This division is made on a empirical basis and dictated by the experience. We identified as “reliable” the color labels “Blue”, “Navy blue”, “Royal blue”, and “Medium blue”. With “reliable”, we mean that these clusters are likely to exhibit a strong dominance of water features with respect to land features. Conversely, we identified as “unreliable” clusters with color label “Midnight blue”. In fact, as shown in Fig. 4, the same color label can be repeated in the same SSOM. These clusters are likely to exhibit a strong dominance of land features with respect to water features.

The splitting of the dictionary led to the result depicted in Fig. 6d. This operation allows for the reconstruction of the reservoir shape using only the clusters of the “unreliable” dictionary (in this case, just the red one) ensuring the preservation of the required scattering and geometric characteristics, discarding all the others.

#### B. Morphological operations on the semantic mask and segmentation

This section describes the blocks indexed from 3 to 6 in Fig. 5.

The masks representative of the “reliable” and of the “unreliable” dictionaries are treated with a morphological filter in order to discard small regions and obtain more homogeneous clusters (see block 3 of Fig. 5) [40]. It is worthwhile to remark that the mask corresponding to the “reliable” dictionary fuses all the color labels belonging to it. In other words, this is a binary “true”/“false” mask in which all the pixels of the SSOM having a color label falling into the “reliable” dictionary are associated to the value “true”. Conversely, the mask associated with the “unreliable” dictionary concerns, at each loop iteration, to just one of its elements.

The objective is to reconstruct the reservoir shape using words. Clusters belonging to the “unreliable” dictionary are added incrementally to the initial nucleus constituted by the “reliable” dictionary and treated with an OBIA dependent on their expected degree of membership to the class “reservoir”. This is dictated by the mean of the SWPP (see Section III-C for more details) computed within the entire cluster. The

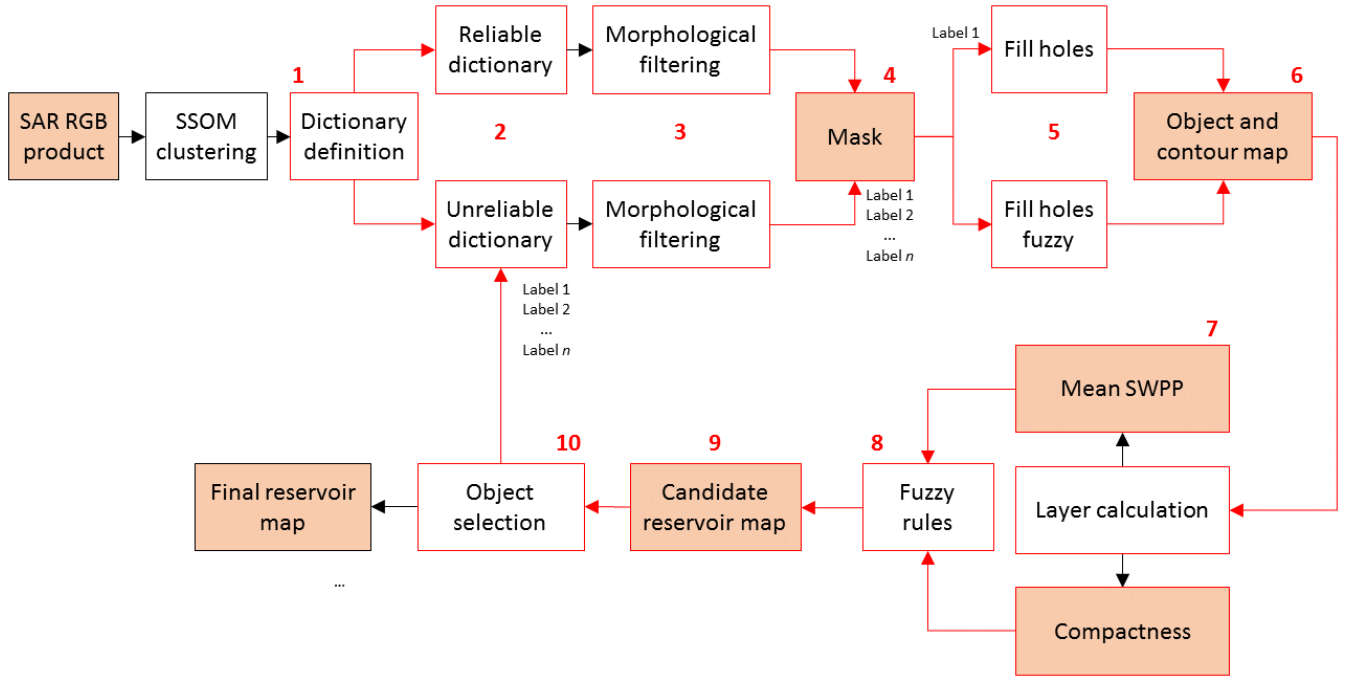


Fig. 5: Small reservoir extraction using SSOM and OBIA: general flowchart. Boxes with filled background represent products. Those with blank background identify processes.

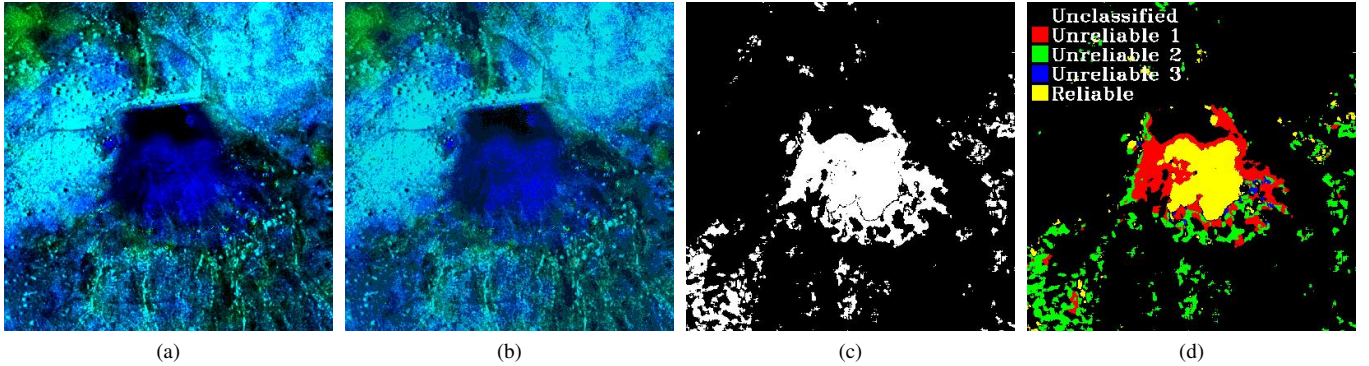


Fig. 6: (a) Sample Level-1 $\alpha$  products concerning a reservoir of the study area, (b) corresponding SSOM, (c) semantic mask obtained considering the whole dictionary, and (d) mask obtained splitting the dictionary in a reliable part (yellow cluster) and in a unreliable part (red, green, and blue clusters). Original patch dimension approximately  $1.5 \times 1.5 \text{ km}^2$ .

higher this value, the higher the probability that the cluster is dominated by water features.

In particular, suppose that our “unreliable” dictionary is composed by three color labels, as in the case of Fig. 6d. They are sorted as the values of the SWPP mean computed cluster-wise and added to the nucleus identified by the “reliable” dictionary in that order. In our case, we have the following situation:  $\langle \text{SWPP} \rangle_{\text{red}} = 0.3$ ,  $\langle \text{SWPP} \rangle_{\text{green}} = 0.28$ ,  $\langle \text{SWPP} \rangle_{\text{blue}} = 0.14$ . This means that, within the loop, the corresponding clusters will be added to the nucleus identified by the “reliable” dictionary (yellow cluster) in the same (descending) order.

As a result, referring to Fig. 6d, at iteration 1 of the loop, the mask considered for object layers calculation is given by the junction of the yellow and red clusters (block 4 of

Fig. 5). It is possible that the output cluster presents several “holes” (i.e. areas not candidate to be classified as reservoir but completely surrounded by candidate objects), and this can alter the calculation of the compactness layer due to the decrease of the ratio between object’s area and perimeter (see Section III-C). This problem is solved in the block indexed with the number 5 in Fig. 5.

In general, the first element of the “unreliable” dictionary (i.e. the one exhibiting the highest SWPP mean) has usually a strong dominance of water features. Therefore, it can be considered a quite “safe” cluster, and its holes treated as islands (due to the clustering or to residual speckle in the original RGB product). In other words, at step 1 of the loop (which concerns the element of the “unreliable” dictionary with the highest SWPP mean), all the holes within the considered

objects are covered using as parameter just the uniqueness of the adjacency to a candidate reservoir cluster.

Starting from the second element of the “unreliable” dictionary and beyond, in which we deal with clusters with a high probability to have a dominant land component, the coverage of possible holes rely on a fuzzy system using as parameters the number of holes and the ratio between their area and the area of the unique candidate object surrounding them. The parameters defining the fuzzy sets exploited in this phase are reported in TABLE I. In particular, we require that holes should be in “low” number, and occupy a “low” area with respect to the one of the object surrounding them.

TABLE I: Adopted fuzzy set parameters for holes filling starting from iteration 2 of the “unreliable” dictionary loop and beyond. The ratio  $A_h/A_o$  indicates the ratio between the area occupied by the holes and the area of the object surrounding them.

Layer	Semantic attribute	Fuzzy set	a	c
Number of holes	Low	Z-type	0	10
Number of holes	High	S-type	5	20
$A_h/A_o$ (%)	Low	Z-type	0	10
$A_h/A_o$ (%)	High	S-type	5	20

Once the mask for the current iteration is assembled, segmentation is implemented in the block 6 of Fig. 5. The object map, indexed with an increasing numeric attribute, is retrieved using a connected components labeling algorithm [41]. Contours are also computed at this stage through the calculation of the image second Laplacian [42]. In fact, objects’ perimeter will be necessary for the calculation of the compactness parameter.

### C. Object layers

This paragraph describes the block indexed with 7 in Fig. 5.

As aforementioned, the fuzzy system devoted to assign the classes “reservoir” and “no reservoir” is fed by two object layers. We use a scattering layer, i.e. the mean seasonal water pseudo-probability (SWPP) calculated within each identified candidate reservoir, and a geometric layer, i.e. the object compactness.

The SWPP is an index measuring the pseudo-probability that a pixel belongs to a temporary water surface. It has been introduced in [36], and computed as follows:

$$\text{SWPP} = \left[ 1 - \left( \frac{G}{255} \right)^2 \right] \frac{B - G}{B + G}, \quad \text{SWPP} \in [-1, 1]. \quad (1)$$

In this formula,  $B$  and  $G$  are the blue and the green band of a Level-1 $\alpha$  product, respectively. Roughly, this formulation aims at the enhancement of areas appearing in blue color in the RGB product. For further details, the reader can refer to [36].

The compactness, as suggested by the name, measures how compact an object is, i.e. how much the object is shaped like a circle. It is defined as follows [39]:

$$C = \frac{4\pi A}{P^2}, \quad C \in ]0, 1]. \quad (2)$$

In this formula,  $A$  and  $P$  represent objects’ area and perimeter, respectively. Indeed, this parameter was introduced to measure the roundness of sand grains, and then reused in the image processing literature. In the digital world, the more compact object is the square, for which  $C = 0.785$ .

### D. Fuzzy rules and candidate objects selection

This section describes the blocks 8 to 10 of Fig. 5.

The two object layers described in Section III-C are combined using fuzzy rules [43], [44]. We used two fuzzy sets, “low” (Z-type) and “high” (S-type), to model the uncertainty related to the considered quantities. Selected parameters for these fuzzy sets are reported in TABLE II.

TABLE II: Adopted parameters to model the fuzzy sets relevant to the mean SWPP computed object-wise and the objects’ compactness.

Layer	Semantic attribute	Fuzzy set	a	c
SWPP	Low	Z-type	0	0.5
SWPP	High	S-type	0.35	0.6
Compactness	Low	Z-type	0	0.15
Compactness	High	S-type	0.05	0.25

Reservoirs are expected to have “high” SWPP mean within candidate objects, which should also exhibit “high” compactness. This combination of the input fuzzy sets leads to the creation of the class “reservoir”. Each object in the segment map will have a certain membership degree to this class. The higher the membership, the higher the probability that the object really represents a reservoir.

However, being the system fuzzy, each of the possible combinations obtainable from the fuzzy sets reported in TABLE II are possible: “High” SWPP plus “High” compactness (i.e. the “reservoir” class), “High” SWPP plus “Low” compactness, “Low” SWPP plus “High” compactness, and “Low” SWPP plus “Low” compactness. The last three classes identify the class “no reservoir”. Each image segment will have a certain membership degree for this class. The higher the membership, the higher the probability that the object belongs to that class. Therefore, a de-fuzzification step is necessary and implemented assigning to each object the class having the maximum probability, given the adopted fuzzy sets.

However, the three classes composing the category “no reservoir” have different probability to really belong to it. In fact, image segments having “High” SWPP plus “Low” compactness have the scattering properties requested for a reservoir, lacking the geometric one. This can be due to residual speckle in the input RGB product altering the response of some area, as well as to clustering, causing the association of some portion of the reservoir to different elements of the “unreliable” dictionary. In other words, some objects belonging to the class “High” SWPP plus “Low” compactness can still be considered for classification as “reservoir” in a successive iteration of the “unreliable” dictionary loop.



This is clarified in Fig. 7, which is an exploded view of the blocks indexed with 9 and 10 in Fig. 5. At the end of iteration 1 (“reliable” dictionary plus first element of the “unreliable” one), objects exhibiting “High” SWPP mean and “High” compactness are stored in the “actual” reservoirs map. Objects having “High” SWPP mean and “Low” compactness are stored into the “maybe” reservoirs map and sent to the second iteration of the “unreliable” dictionary loop, in which the second element of this dictionary is added to the already retrieved semantic mask. After fuzzy classification, objects within the “maybe” reservoirs acquiring the characteristics of “High” SWPP mean and “High” compactness, are transferred in the “actual” reservoirs map. Obviously, objects having “High” SWPP and “High” compactness also appear in the “maybe” reservoir map. In fact, they can be updated by the addition of other elements of the “unreliable” dictionary, provided that the fusion preserves these characteristics. In other words, if the addition of new image segments to an object having “High” SWPP and “High” compactness creates an object still having “High” SWPP and “High” compactness, this new object is stored in the “actual” reservoirs map. Otherwise, it is discarded, and the old object restored.

The loop is repeated for each element of the “unreliable” dictionary up to its depletion. At the end of the loop, the “actual” reservoirs map becomes the “final” reservoirs map.

#### E. Study area, data, and ground truth

The study area is located in a rural area of Burkina Faso (Western Africa). It is about  $36 \times 18$  km wide, and land cover is prevalently natural, with just few villages scattered into the scene. Data were provided by the Italian Space Agency at free of charge under the aegis of the “HydroCIDOT” project. In particular, our database is constituted by more than 50 COSMO-SkyMed stripmap three meter resolution images acquired in HH polarization between 2010 and 2016. The interested reader can find further information about this dataset in [36].

In our study area, a different number of reservoirs can be observed (with a maximum 13, ranging approximately from 6000 to 300000 m<sup>2</sup> of extension) depending on the period of the year. In fact, in semi-arid environment, starting from the end of the wet season, reservoirs tend to recede up to completely disappear with the advance of the dry season. This makes their identification even more challenging. In fact, we are analyzing ponds whose boundaries are not man-made. Therefore, there is no clear edge between the water surface and the surrounding land. Moreover, their tendency to dry creates further ambiguity due to the presence of mud at the boundary, especially during the transition from the wet to the dry season.

The ground truth used to assess the obtained results was manually retrieved for each considered acquisition. This operation was not trivial, due to the strong unbalance between the classes water and non-water and the presence of vegetation/mud at reservoir boundary making it difficult to recognize the contour. However, in many cases, the expert photo-interpretors are able to perform reliable feature extraction [45], [46], especially if they have a good *a priori* knowledge of

the study area [29], [37], [47]. This makes us quite confident that the reservoir contours manually retrieved through photo-interpretation are well representative of the real basins extension.

#### F. Experimental results

In this Section we present the results of the proposed framework application to 8 images taken from the available database. Acquisition dates were selected with the purpose to catch the most important moments of reservoirs’ life-cycle, i.e. the maximum extension towards the peak of the wet season (July-August), and the starting of the recession in the transition between the wet and the dry seasons (September-October).

An important parameter of the proposed method, which can significantly condition its performance, is the number of clusters in the input SSOM. Actually, the optimum number of clusters in unsupervised clustering is an open problem [48]–[50]. Therefore, we adopted an empiric approach. In particular, we repeated the reservoirs extraction experiment changing the number of clusters in the SSOM, setting it to 25, 36, 49 and 64 clusters. In all cases, the same dictionary was used. Results of these experiments are reported in TABLE III. A pixel-based and a object-based assessment of the performance of the proposed methodology were implemented. As for the object-based assessment, an object is considered hit if it is detected for more than 30% of its total extension.

Main outcomes of the performed experiments are the followings. As aforementioned, the number of clusters set in the input SSOM can greatly affect the detection of the reservoirs. We found that setting it to 25 or 36 lead to conflicting results, sometimes very unpleasant. In fact, in these cases, the “unreliable” dictionary does not have clusters with dominant water features. Therefore, the fusion around the nucleus constituted by the “reliable” dictionary of image segments mainly representing land, causes the loss of the scattering and geometric properties (defined in Section III-C) required to candidate objects to be classified as reservoirs.

The proposed method performs at its best raising the number of clusters in the input SSOM. In fact, setting it to 49 or 64, the clustering is able to model appropriately the transition between water and land features at reservoirs boundary creating image segments representative of this intermediate land cover, thus allowing for a satisfying reconstruction of the reservoirs shape.

The principal characteristic of the proposed architecture is the very low probability of false alarms. In fact, the maximum number of false reservoirs detected in the performed experiments is 4 on 31 August 2010, using the 36-cluster SSOM. Using the 64-cluster SSOM, this value decreases to 2. Averaging the results of all the experiments, the results we obtain are the followings: 25-cluster, 1.125 false reservoirs per image; 36-cluster, 1.125 false reservoirs per image; 49-cluster, 0.875 false reservoirs per image; 64-cluster, 0.75 false reservoirs per image.

Missed detections are mainly due to: i) the application of morphological operators for cluster regularization causing erosion of objects’ boundary (this causes missed detection only at the pixel level); ii) the presence of clusters having dominant

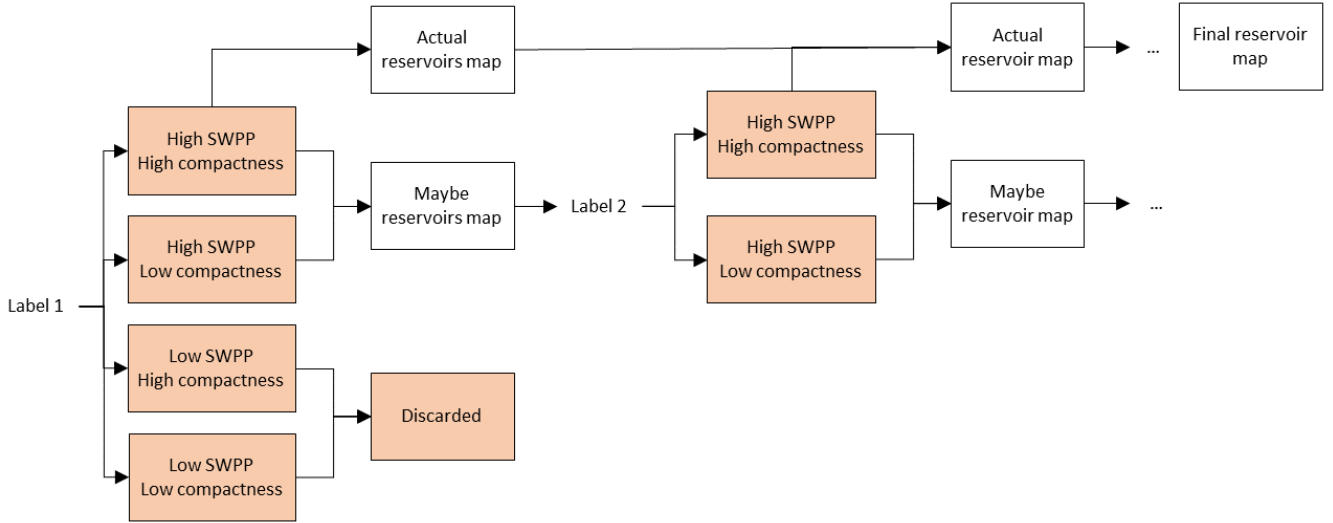


Fig. 7: “Unreliable” dictionary loop management. At the end of iteration 1 objects exhibiting “High” SWPP mean and “High” compactness are stored in the “actual” reservoirs map. Objects having “High” SWPP mean and “Low” compactness are stored into the “maybe” reservoirs map and sent to the second iteration of the loop. After fuzzy classification rules, objects acquiring the characteristics of “High” SWPP mean and “High” compactness, are added to the “actual” reservoirs map. Boxes with filled background represent products. Those with blank background identify processes.

TABLE III: Results of the application of the proposed framework for 8 images of the available dataset and for different number of clusters in the input SSOM.  $N$ : number of SSOM clusters, OA: overall accuracy, FA: false alarm rate. P: pixel-based assessment, O: object-based assessment.

Date	$N$	OA		FA		Date	$N$	OA		FA	
		P (%)	O	$P \times E^{-4}$	O			P (%)	O	$P \times E^{-4}$	O
2010/07/14	25	25.9	7/9	1.21	1	2011/10/09	25	86.2	11/11	0.36	1
	36	24.9	7/9	0.73	1		36	85.2	11/11	0.32	1
	49	82.6	9/9	1.18	3		49	83.9	11/11	0.36	1
	64	90.2	9/9	1.14	2		64	85.0	11/11	0.24	0
2010/08/31	25	84.6	13/13	0.52	2	2014/07/01	25	39.6	6/8	1.48	3
	36	84.7	13/13	0.57	4		36	40.3	6/8	1.70	2
	49	83.7	13/13	0.15	1		49	83.2	8/8	2.58	2
	64	83.4	13/13	0.35	2		64	89.0	8/8	2.70	2
2010/09/16	25	86.5	13/13	0.61	0	2014/08/26	25	29.4	7/10	0.80	0
	36	88.8	13/13	0.73	0		36	87.1	9/10	1.10	0
	49	85.0	13/13	0.66	0		49	86.0	9/10	0.80	0
	64	84.9	13/13	0.38	0		64	82.0	9/10	0.71	0
2011/09/03	25	37.4	10/11	0.61	0	2014/10/05	25	86.1	10/10	1.38	2
	36	35.2	10/11	0.55	0		36	84.5	10/10	1.02	1
	49	86.1	11/11	0.22	0		49	76.0	9/10	0.60	0
	64	88.5	11/11	0.49	0		64	86.5	10/10	0.63	0

land features at reservoirs borders causing the rejection of the retrieved object by the fuzzy system described Section III-D; iii) the presence, especially at reservoirs’ boundary, of clusters having color label not included into the “reliable”/“unreliable” dictionary.

A graphical explanation of the method behavior is provided in Fig. 8. In particular, in Fig. 8a, we report a 64-cluster SSOM centered on a reservoir of the study area. It is the only reservoir missed using the 64-cluster SSOM in the performed experiments (see TABLE III, acquisition on 26 August 2014). In Fig. 8b, the mask obtained at iteration 1 of the “unreliable”

dictionary loop is shown. In this case, the presence of vegetation within the basin can not be compensated by the “fill holes” procedure because the correspondent “holes” are connected with the background, i.e. not completely surrounded by white pixels. This situation is maintained for all the iterations of the “unreliable” dictionary loop and causes the lost of the compactness requirement asked to the shape to be classified as a reservoir.

In Fig. 9, we provide another graphical example of the behavior of our method, this time oriented to the pixel level. In particular, in Fig. 9a, a 64-cluster SSOM representing two

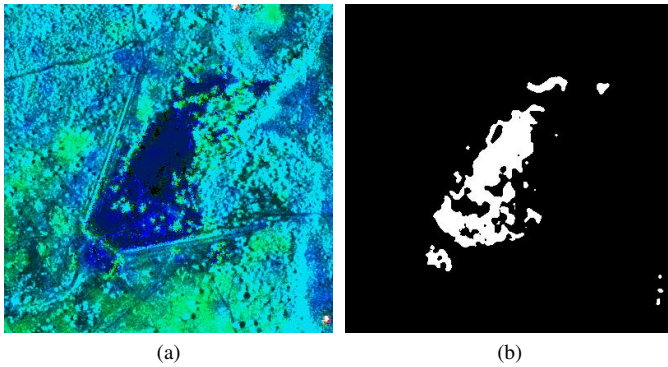


Fig. 8: (a) 64-cluster SSOM. (b) Mask obtained after the first iteration of the “unreliable” dictionary loop. The presence of areas connected to the background causes the loss of the compactness requirement. Original patch dimension approximately  $1.5 \times 1.5 \text{ km}^2$ .

reservoirs of the study area is shown. In Fig. 9b, a classification map is depicted. Green, red, and yellow colors mean correct decision, missed detections and false alarms, respectively. Considering the larger of the two reservoirs, there is a stripe (wider on the left) which is missed in the computed mask. This is because this stripe mainly falls in the cluster labeled as “Dark slate gray”, which is generally not associated to the reservoir class and therefore not included in our dictionaries.

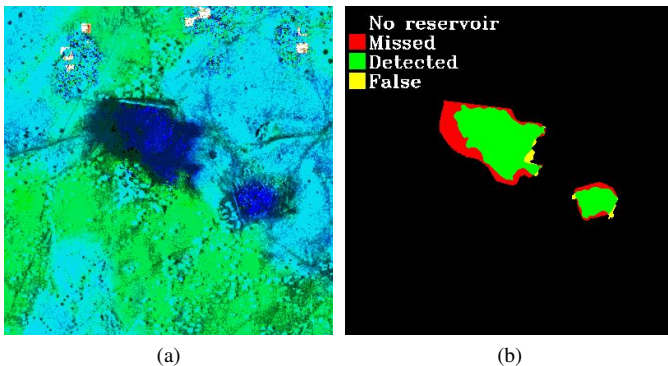


Fig. 9: (a) 64-cluster SSOM (b) Classification map. Green: correct detections. Red: missed detections. Yellow: false detections. Original patch dimension approximately  $1.5 \times 1.5 \text{ km}^2$ .

As for pixel-based false alarms, the mechanism is quite similar. They can occur if, within the “unreliable” dictionary loop, a small image segment mixing water and land features is added to the “master” object. In this case (see yellow pixels in Fig. 8b), land features, being strongly minority, does not affect the properties of the object and are aggregated to it to form the final shape classified as reservoir.

### G. Comparison with other methods

In this Section, we compare the results obtained using the proposed methodology with other popular classification

methods. We assume as reference the experiments using the 64-cluster SSOM as input, which are those giving the best trade-off between overall accuracy and false alarms.

The comparison is made with other (pixel-based) methods, very popular among end-users and widely available on commercial/open-source software suites for remote sensing data analysis. In particular, we tested the performance of the maximum-likelihood (ML) classifier, of the support-vector machine (SVM), and of a standard back-propagation neural net (NN). We also implemented the reservoirs extraction through binary segmentation of the the seasonal water pseudo-probability map recently introduced by the authors [36]. Finally, we experimented the multiresolution image segmentation algorithm (MR) [51] coupled with an object-based analysis made on a single layer, given by the mean of the ratio image calculated segment-wise, which is treated with hard thresholding to classify. All these techniques were applied to the Level-1 $\alpha$  products used as input for SSOM clustering. In fact, the authors demonstrated that the performance of standard classifiers when applied to Level-1 $\alpha$  and Level-1 $\beta$  products are fully comparable with those given by their application to standard temporal-filtered SAR images (see, as an example, [20], [36], [40], [44] for more details).

As for ML, SVM, and NN techniques, 4-class classifications (water, bare soil, layover, and vegetation) were implemented. It is worthwhile to remark that they are supervised classifiers (while the proposed method, after the definition of the dictionary, is fully unsupervised). Therefore, for each of the considered acquisitions, relevant training samples for each class (about 10% of the ground truth) were selected. As for the SWPP, the threshold value to be applied to the pseudo-probability map was retrieved through a trial-and-error approach. As explained in [36], this value is not time-dependent if the same reference image is used to build the time series of Level-1 $\alpha$  products.

The results of the performed experiments are summarized in TABLE IV and TABLE V. As first, we analyze TABLE IV. Compared to the other considered classifiers, the proposed methodology systematically reduces the false alarm rate. On the other hand, the object-based overall accuracy is slightly lower. This means that, generally, a pixel-based classifier allows for having better performances at the border of the reservoir, but at the cost of a higher false alarm rate, which may be significant in some cases. This happens especially for the ML classifier on 1 July 2014 and 26 August 2014, and for the NN classifier on 1 July 2014. These classifications are completely failed, despite an expert selection of the training samples. In general, we think that the best trade-off between the accuracy and the false alarms is given, between the considered techniques, by the SVM classification, whose performance are almost inline with those of the proposed methodology.

As for the MR-based procedure, the obtained results are quite satisfying. In fact, the overall accuracy is in line with those of the best performing methods, while data on false alarms confirmed the robustness of OBIA techniques with respect to this quality parameter. Principal drawbacks of this experiment are the fine tuning necessary to find the best

TABLE IV: Comparison between the proposed algorithm and other popular classification methods: seasonal water pseudo-probability (SWPP), maximum likelihood (ML), support vector machine (SVM), neural net (NN), multiresolution segmentation (MR). N: applied threshold for binary segmentation or number of clusters/classes for supervised classifiers. OA: overall accuracy, FA: false alarm rate. P: pixel-based assessment. O: object-based assessment. Bold characters indicate the best registered performance.

Date	Method	N	OA		FA		Date	Method	N	OA		FA	
			P (%)	O	$P \times E^{-4}$	O				P (%)	O	$P \times E^{-4}$	O
2010/07/14	Proposed	64	90.2	9/9	1.14	2	2011/10/09	Proposed	64	85.0	11/11	<b>0.24</b>	0
	SWPP	0.3	94.9	9/9	3.04	20		SWPP	0.3	89.5	11/11	0.47	2
	ML	4	94.4	9/9	1.38	5		ML	4	78.8	11/11	3.50	40
	SVM	4	92.4	9/9	<b>1.18</b>	5		SVM	4	85.8	11/11	0.33	2
	NN	4	<b>95.0</b>	9/9	1.62	4		NN	4	<b>89.9</b>	11/11	0.29	1
	MR	2.5	90.0	9/9	1.73	2		MR	2.5	87.6	11/11	0.72	0
2010/08/31	Proposed	64	83.4	13/13	<b>0.35</b>	2	2014/07/01	Proposed	64	89.0	8/8	<b>2.70</b>	2
	SWPP	0.3	<b>89.8</b>	13/13	1.35	12		SWPP	0.3	91.8	8/8	4.45	12
	ML	4	89.3	13/13	0.95	8		ML	4	<b>98.3</b>	8/8	594	2069
	SVM	4	88.4	13/13	0.18	3		SVM	4	89.8	8/8	5.87	21
	NN	4	85.5	13/13	1.08	9		NN	4	93.1	8/8	33.6	226
	MR	2.5	77.0	11/13	0.66	2		MR	2.5	88.3	8/8	3.20	0
2010/09/16	Proposed	64	84.9	13/13	<b>0.38</b>	0	2014/08/26	Proposed	64	82.0	9/10	0.71	0
	SWPP	0.3	<b>90.2</b>	13/13	0.76	3		SWPP	0.3	92.8	10/10	1.38	5
	ML	4	<b>90.2</b>	13/13	1.60	3		ML	4	<b>96.4</b>	10/10	22.4	122
	SVM	4	78.6	13/13	0.43	1		SVM	4	87.9	10/10	<b>0.70</b>	2
	NN	4	83.5	13/13	0.52	2		NN	4	91.8	10/10	0.89	3
	MR	2.5	66.8	12/13	0.59	1		MR	2.5	86.0	10/10	1.22	1
2011/09/03	Proposed	64	88.3	11/11	0.49	0	2014/10/05	Proposed	64	86.5	10/10	<b>0.63</b>	2
	SWPP	0.3	89.1	11/11	0.60	2		SWPP	0.3	90.2	10/10	1.60	6
	ML	4	90.3	11/11	1.38	8		ML	4	<b>96.6</b>	10/10	2.96	11
	SVM	4	86.9	11/11	<b>0.41</b>	1		SVM	4	87.6	10/10	1.39	6
	NN	4	<b>90.2</b>	11/11	1.83	12		NN	4	88.4	10/10	1.51	6
	MR	2.5	87.4	11/11	0.93	0		MR	2.5	84.3	9/10	1.64	1

parameter setup for the MR algorithm and the trial-and-error approach to determine the hard threshold to be applied to the considered object layer.

Another useful tool to evaluate the performance of all the analyzed methods is provided in TABLE V, in which aggregated results are reported. In particular, we considered the mean pixel-based overall accuracy and the median of the object-based false alarm computed considering the results for the 8 performed experiments. The median is chosen to exclude outliers from the assessment.

TABLE V: Summary of the obtained results. AOA: average pixel-based overall accuracy. MFA: Median of the object-based false alarm. Bold characters indicate the best registered performance.

Method	AOA (pixel)	MFA (object)
Proposed	86.2%	<b>0</b>
SWPP	91.0%	5.5
ML	<b>91.8%</b>	9.5
SVM	87.2%	2.5
NN	89.7%	5
MR	83.4%	1

From the first column of the table, it arises that the overall

accuracy is (on average) comparable and rather high for all the considered methods, ranging from the 83.4% of the OBIA based on multiresolution segmentation to the 91.8% of the ML. The value for the proposed method is 86.2%, and it is in line with that registered for the SVM, which is 87.2%, so just one point above the one given by our technique.

As for the second column, it is remarkable that the proposed method restitutes a median of false alarms equal to zero. MR and SVM also gives satisfying results, having a median of false alarms of 1 and 2.5, respectively, with no particularly serious outliers (see TABLE IV). The NN and the SWPP perform pretty well with a median of about 5. However, in the case of the NN, one of the experiments we made resulted failed. The ML classifier gave the worst performance with respect to this indicator, and its usage for this application is seriously compromised by the probability of failed classifications.

Summarizing, the proposed method showed performance comparable with those of popular pixel-based supervised techniques (ML, SVM, NN) in terms of accuracy, with the advantages of minimizing false alarms (thanks to object-based processing) and of being unsupervised (after the dictionary definition). This makes our method very well suited for the analysis of long time series, where robustness with respect to misclassification is crucial due to the scarce supervision

TABLE VI: Contribution of the three technique’s module to the final result. Step 1: semantic pre-classification mask based on the “reliable” dictionary. Step 2: first OBIA iteration. Step 3: other OBIA iterations. OA: overall accuracy. FA: false alarms. In the OA column, we report in parenthesis the percentage value of the module contribution with respect to the total.

Acquisition date	Step 1		Step 2		Step 3	
	OA (%)	$FA \times E^{-4}$	OA (%)	$FA \times E^{-4}$	OA (%)	$FA \times E^{-4}$
2010/07/14	50.5 (56.0)	221	89.0 (42.7)	0.09	90.2 (1.33)	1.14
2010/08/31	44.7 (53.6)	70.1	82.0 (44.7)	0.02	83.4 (1.67)	0.35
2010/09/16	46.4 (54.6)	79.4	83.8 (44.0)	0.02	84.9 (1.29)	0.38
2011/09/16	46.2 (52.3)	77.2	74.4 (32.0)	0.02	88.3 (15.7)	0.49
2011/10/09	49.2 (57.9)	19.4	83.7 (40.5)	0.01	85.0 (1.52)	0.24
2014/07/01	48.9 (54.9)	118	87.0 (42.8)	1.07	89.0 (2.24)	2.70
2014/08/26	45.9 (55.9)	80.1	80.9 (42.6)	0.06	82.6 (1.34)	0.71
2014/10/15	40.9 (47.3)	43.3	83.8 (49.6)	0.05	86.5 (3.12)	0.63

(which is the main weakness of current OBIA methods, like the one based on MR here analyzed). Moreover, in this application, supervised techniques have a double drawback: i) the necessity of selecting relevant training samples for each image to be classified and/or the fine tuning phase for the best technique’s parameter set-up, and ii) the strong dependency of the classification result from the quality of such training sets/parameters, which makes the operation highly dependent on the expertise of the operator.

#### H. Modules contribution

The proposed method can be packed into three steps: i) the semantic pre-classification mask constituted by the “reliable” dictionary; ii) the first OBIA iteration using the first element of the “unreliable” dictionary; iii) the successive iterations of the OBIA loop, from the second to the last element of the “unreliable” dictionary. The purpose of this section is to evaluate quantitatively the contribution of each module to the final result. The outcomes of this investigation are reported in TABLE VI concerning the pixel-based overall accuracy and false alarm rate. In the overall accuracy column, we report in parenthesis the percentage value of the module contribution with respect to the total.

As a general comment, the first step (i.e. the pixel-based analysis of the “reliable” dictionary), brings an average contribution of about 53% to the total detections. In this phase, the false alarm is quite high, since no OBIA has been implemented yet. The second step accounts for about 42% of the total detections. However, in this phase, a significant reduction of false alarms is achieved thanks to OBIA. The last step is in most cases just a refinement, allowing to better delineate reservoir borders with negligible increase of false alarms. Only in one case a significant improvement of the detection rate was registered in this processing phase (see experiment relevant to the acquisition of 2011/09/16).

#### I. Sensitivity analysis

In this section, the sensitivity analysis of the performance of the method with respect to variations of its parameters is presented.

Actually, being the problem of the number of clusters to be set in the SSOM already discussed before, the parameters

we considered here for the assessment are those defining the fuzzy system ruling the object layers and the filling holes operation. Therefore, we changed the parameters reported in TABLE II and TABLE I of  $\pm 5\%$  and  $\pm 10\%$ . Results of these new experiments are shown in TABLE VII for the 64-cluster SSOM case. In particular, the experiments  $F_{-5}$ ,  $F_{-10}$ ,  $F_{+5}$ , and  $F_{+10}$  have been implemented changing the parameters of  $-5\%$ ,  $-10\%$ ,  $+5\%$ , and  $+5\%$ , respectively. Reference results are named as  $F_0$ .

The obtained results show a very poor sensitivity of the method on its parameters. In fact, their decreasing, up to 10%, does not affect significantly the false alarm rate. As an example, the mean of the object-based false alarms passes from a value of 1 in the case of “optimum” parameter selection (see TABLE II and TABLE I) to about 1.9 for both  $F_{-5}$  and  $F_{-10}$  experiments. Similarly, raising all the parameters of 10% has a very negligible impact on the overall accuracy.

## IV. CONCLUSIONS

One of the challenges of modern remote sensing is the integration of perceptive insights and mathematics for building user-oriented processing chains allowing for fully exploitation of Earth observation in operational/industrial contexts. In this work, we have presented a novel architecture for feature extraction from multitemporal SAR data mixing classic SAR processing and GEOBIA concepts. It was based on the usage of the recently introduced RGB products of the Level-1 $\alpha$  and Level-1 $\beta$  families. These images have been treated with a self-organized map algorithm derived from the classic Kohonen’s schema and opportunely modified to best fit the characteristics of the input products and to make it possible the automatic attachment of a basic semantics to each cluster of the output feature space.

The available semantics, referring to clusters’ color, has been used to build a dictionary related to the feature of interest, represented in the example discussed in Section III by small reservoirs in semi-arid environment. The dictionary was then split in a “reliable” and a “unreliable” part. The former included color labels which are likely to exhibit dominant water features. The latter is composed by clusters which could have dominance of land pixels.

The “reliable” dictionary was used as a nucleus to reconstruct the reservoirs shape within a loop, in which the

TABLE VII: Assessment of the performance of the proposed method with respect to variations of the parameters governing the fuzzy systems for object-layers management and filling holes operation. Reference results: experiment  $F_0$ . Experiments  $F_{-5}$ ,  $F_{-10}$ ,  $F_{+5}$ , and  $F_{+10}$  have been run with parameters lowered of 5% and 10%, and raised of 5% and 10%, respectively. OA: overall accuracy, FA: false alarm rate. P: pixel-based assessment, O: object-based assessment.

Date	$F$	OA		FA		Date	$F$	OA		FA	
		P (%)	O	$P \times E-4$	O			P (%)	O	$P \times E-4$	O
2010/07/14	$F_{-0}$	90.2	9/9	1.14	2	2011/10/09	$F_{-0}$	85.0	11/11	0.24	0
	$F_{-5}$	90.2	9/9	1.89	3		$F_{-5}$	85.0	11/11	0.24	0
	$F_{+5}$	90.2	9/9	1.14	2		$F_{+5}$	85.0	11/11	0.24	0
	$F_{-10}$	90.2	9/9	1.94	3		$F_{-10}$	85.0	11/11	0.24	0
	$F_{+10}$	90.2	9/9	1.14	2		$F_{+10}$	85.0	11/11	0.24	0
2010/08/31	$F_{-0}$	83.4	13/13	0.35	2	2014/07/01	$F_{-0}$	89.0	8/8	2.70	2
	$F_{-5}$	83.4	13/13	0.50	3		$F_{-5}$	89.0	8/8	3.05	4
	$F_{+5}$	83.4	13/13	0.27	1		$F_{+5}$	89.0	8/8	2.50	2
	$F_{-10}$	83.4	13/13	0.50	3		$F_{-10}$	89.0	8/8	3.44	4
	$F_{+10}$	83.4	13/13	0.27	1		$F_{+10}$	89.0	8/8	2.50	2
2010/09/16	$F_{-0}$	84.9	13/13	0.38	0	2014/08/26	$F_{-0}$	82.0	9/10	0.71	0
	$F_{-5}$	85.4	13/13	0.38	0		$F_{-5}$	87.7	10/10	0.82	3
	$F_{+5}$	84.9	13/13	0.38	0		$F_{+5}$	82.0	9/10	0.66	0
	$F_{-10}$	85.4	13/13	0.38	0		$F_{-10}$	87.7	10/10	0.82	3
	$F_{+10}$	84.9	13/13	0.38	0		$F_{+10}$	82.0	9/10	0.66	0
2011/09/03	$F_{-0}$	88.3	11/11	0.49	0	2014/10/05	$F_{-0}$	86.5	10/10	0.71	2
	$F_{-5}$	88.3	11/11	0.49	0		$F_{-5}$	86.9	10/10	0.71	2
	$F_{+5}$	88.3	11/11	0.49	0		$F_{+5}$	86.5	10/10	0.71	2
	$F_{-10}$	89.0	11/11	0.66	0		$F_{-10}$	86.9	10/10	0.71	2
	$F_{+10}$	88.3	11/11	0.49	0		$F_{+10}$	84.5	10/10	0.53	2

elements of the “unreliable” dictionary were added one by one based on the probability they have to represent clusters with dominant water features. This allowed for building a semantic mask of candidate image segments. Two object-layers have been introduced to individuate, among them, those having the scattering and geometric characteristics best fitting those of a reservoir. They were the mean (computed object-wise) of the seasonal water pseudo-probability (scattering layer) and the compactness (geometric layer). A fuzzy system rules the selection/rejection of candidate reservoirs.

The performance of the proposed architecture has been compared with that of popular pixel-based supervised classifiers and with that of an object-based approach based on a literature segmentation method. As a result, using our method we registered a significant improvement of the robustness to false alarms, keeping a comparable detection accuracy.

A sensitivity analysis on the parameters defining the fuzzy classification system was also performed. The results show that the proposed architecture is quite insensitive to variations, even significant, of its parameters.

The proposed methodology represents a robust unsupervised tool for time series analysis and can be adapted to several remote sensing problems, provided the definition of the dictionary best representing the scattering characteristics of the feature of interest and of the most suitable object-based image analysis for its identification.

#### ACKNOWLEDGMENTS

The authors thank the Italian Space Agency (ASI) for providing the Burkina Faso dataset under the aegis of the “HydroCIDOT” project.

#### REFERENCES

- [1] V. Madhok and D. A. Landgrebe, “A Process Model for Remote Sensing Data Analysis,” *IEEE Trans. Geosci. Remote Sens.*, vol. 40, no. 3, pp. 680–686, 2002.
- [2] S. D. Kushnir, C. H. Heithecker, J. A. Ballas, and D. C. McFarlane, “Situation assessment through collaborative human-computer interaction,” *Naval Engineers Journal*, vol. 108, no. 4, pp. 41–51, 1996.
- [3] D. M. J. McKeown, S. D. Cochran, S. J. Ford, J. C. McGlone, J. A. Shufelt, and D. A. Yocum, “Fusion of HYDICE hyperspectral data with panchromatic imagery for cartographic feature extraction,” *IEEE Trans. Geosci. Remote Sens.*, vol. 37, no. 3, pp. 1261–1277, 1999.
- [4] M. Datcu and K. Seidel, “Human-Centered Concepts for Exploration and Understanding of Earth Observation Images,” *IEEE Trans. Geosci. Remote Sens.*, vol. 43, no. 3, pp. 52–59, 2005.
- [5] D. Amitrano, G. Di Martino, A. Iodice, D. Riccio, and G. Ruello, “A New Framework for SAR Multitemporal Data RGB Representation: Rationale and Products,” *IEEE Trans. Geosci. Remote Sens.*, vol. 53, no. 1, pp. 117–133, 2015.
- [6] M. Nagao and T. Matsuyama, *A Structural Analysis of Complex Aerial Photographs*. New York: Plenum Press, 1980.
- [7] R. A. Brooks, “Symbolic Reasoning Among 3-D Models and 2-D Images,” *Artificial Intelligence*, no. 1-3, pp. 285–348, 1981.
- [8] T. Matsuyama and V. S.-H. Hwang, *SIGMA - A Knowledge-Based Aerial Image Understanding System*. New York: Plenum Press, 1990.
- [9] G. J. Hay and G. Castilla, *Geographic Object-Based Image Analysis (GEOBIA): A new name for a new discipline*. Berlin, Heidelberg: Springer, 2008, pp. 75–89.
- [10] S. Lang, “Object-based image analysis for remote sensing applications: Modeling reality - dealing with complexity,” in *Object-Based Image Analysis - Spatial Concepts for Knowledge-Driven Remote Sensing Applications*, T. Blaschke, S. Lang, and G. J. Hay, Eds. Berlin, Germany: Springer-Verlag, 2008, pp. 3–28.

- [11] B. Aksoy and M. Ercanoglu, "Landslide identification and classification by object-based image analysis and fuzzy logic: An example from the Azdavay region (Kastamonu, Turkey)," *Comput. Geosci.*, vol. 38, pp. 87–98, 2012.
- [12] T. Blaschke, B. Feizizadeh, and D. Holbling, "Object based image analysis and digital terrain analysis for locating landslides in the Urmia Lake basin, Iran," *IEEE J. Sel. Topics Appl. Earth Observ.*, vol. 7, no. 12, pp. 4806–4817, 2014.
- [13] B. Aiazzi, L. Alparone, S. Baronti, A. Garzelli, and C. Zoppetti, "Nonparametric Change Detection in Multitemporal SAR Images Based on Mean-Shift Clustering," *IEEE Trans. Geosci. Remote Sens.*, vol. 51, no. 4, pp. 2022–2031, 2013.
- [14] H. Skriver, F. Mattia, G. Satalino, A. Balenzano, V. Pauwels, N. Verhoest, and M. Davidson, "Crop Classification Using Short-Revisit Multitemporal SAR Data," *IEEE J. Sel. Topics Appl. Earth Observ.*, vol. 4, no. 2, pp. 423–431, 2011.
- [15] N. Longbotham, F. Pacifici, T. Glenn, A. Zare, M. Volpi, D. Tuia, E. Christophe, J. Michel, J. Inglada, J. Chanussot, and Q. Du, "Multi-Modal Change Detection, Application to the Detection of Flooded Areas: Outcome of the 2009 Data Fusion Contest," *IEEE J. Sel. Topics Appl. Earth Observ.*, vol. 5, no. 1, pp. 331–342, 2012.
- [16] J. Lu, J. Li, G. Chen, L. Zhao, B. Xiong, and G. Kuang, "Improving pixel-based change detection accuracy using an object-based approach in multitemporal sar flood images," *IEEE J. Sel. Topics Appl. Earth Observ.*, vol. 8, no. 7, pp. 3486–3496, 2015.
- [17] S. Lobry, L. Denis, and F. Tupin, "Multitemporal sar image decomposition into strong scatterers, background, and speckle," *IEEE J. Sel. Topics Appl. Earth Observ.*, vol. 9, no. 8, pp. 3419–3429, 2016.
- [18] T. Kohonen, *Self-Organizing Maps*. Berlin, Heidelberg: Springer-Verlag, 2001.
- [19] T. Blaschke, "Object based image analysis for remote sensing," *ISPRS J. Photogramm. Remote Sens.*, vol. 65, no. 1, pp. 2–16, 2010.
- [20] D. Amitrano, G. Cecinati, G. Di Martino, A. Iodice, P.-P. Mathieu, D. Riccio, and G. Ruello, "Multitemporal Level-1 $\beta$  Products: Definitions, Interpretation, and Applications," *IEEE Trans. Geosci. Remote Sens.*, vol. 54, no. 11, pp. 6545–6562, 2016.
- [21] C. Knoth and D. Nüst, "Reproducibility and Practical Adoption of GEOBIA with Open-Source Software in Docker Containers," *Remote Sens.*, vol. 9, no. 3, p. 290, 2017.
- [22] D. Amitrano, G. Di Martino, A. Iodice, D. Riccio, and G. Ruello, "RGB SAR Products: Methods and Applications," *European Journal of Remote Sensing*, vol. 49, pp. 777–793, 2016.
- [23] B. C. Hewitson and R. G. Crane, "Self-organizing maps: applications to synoptic climatology," *Climate Res.*, vol. 22, pp. 13–26, 2002.
- [24] P. T. Pearson and C. I. Cooper, "Using Self Organizing Maps to Analyze Demographics and Swing State Voting in the 2008 U.S. Presidential Election," in *Artificial Neural Networks in Pattern Recognition*, ser. Lecture Notes in Computer Science, N. Mana, F. Schwenker, and E. Trentin, Eds. Springer Berlin Heidelberg, 2012, vol. 7477, pp. 201–212.
- [25] K. Kiviluoto, "Predicting bankruptcies with the self-organizing map," *Neurocomputing*, vol. 21, no. 1-3, pp. 191–201, 1998.
- [26] M. L. Gonçalves, J. A. F. Costa, and M. L. A. Netto, "Land-Cover Classification Using Self-Organizing Maps Clustered with Spectral and Spatial Information," in *Self Organizing Maps - Application and Novel Algorithm Design*, J. I. Mwasiagi, Ed. InTech, 2011, pp. 299–322.
- [27] M. M. Kamal, P. J. Pasmore, and I. D. H. Shepherd, "Integration of geographic information system and RADARSAT synthetic aperture radar data using a self-organizing map network as compensation for real-time ground data in automatic image classification," *Journal Appl. Remote Sens.*, vol. 4, no. 1, pp. 1–13, 2010.
- [28] S. Patra and L. Bruzzone, "A Novel SOM-SVM-Based Active Learning Technique for Remote Sensing Image Classification," *IEEE Trans. Geosci. Remote Sens.*, vol. 52, no. 11, pp. 606–616, 2014.
- [29] D. Amitrano, G. Di Martino, A. Iodice, D. Riccio, G. Ruello, M. N. Papa, F. Ciervo, and Y. Koussoubé, "Effectiveness of high-resolution SAR for water resource management in low-income semi-arid countries," *Int. J. Remote Sens.*, vol. 35, no. 1, pp. 70–88, 2014.
- [30] D. Amitrano, F. Cecinati, G. Di Martino, A. Iodice, P.-P. Mathieu, D. Riccio, and G. Ruello, "Multitemporal Synthetic Aperture Radar for Urban Planning and Critical Infrastructure Monitoring," in *IEEE Joint Urban Remote Sensing Event*, 2015.
- [31] E. Boelee, P. Cecchi, and A. Kone, "Health Impacts of Small Reservoirs in Burkina Faso," International Water Management Institute, Colombo, Sri Lanka, IWMI Working Paper 136, 2009.
- [32] P. Cecchi, A. Meunier-Nikiema, N. Moiroux, and B. Sanou, "Towards an atlas of lakes and reservoirs in burkina," in *Small reservoir toolkit*, M. Andreini, M. Schuetz, T. Harrington, and L. Battaramulla, Eds. Colombo: International Water Management Institute, 2009.
- [33] J. Liebe, N. van de Giesen, M. Andreini, T. Steenhuis, and M. Walter, "Suitability and Limitations of ENVISAT ASAR for Monitoring Small Reservoirs in a Semiarid Area," *IEEE Trans. Geosci. Remote Sens.*, vol. 47, no. 5, pp. 1536–1547, 2009.
- [34] J. Liebe, N. van de Giesen, and M. Andreini, "Estimation of small reservoir storage capacities in semi-arid environment: A case study in the Upper East Region of Ghana," *Phys. Chem. Earth Pt. A/B/C*, vol. 30, pp. 448–454, 2005.
- [35] T. Sawunyama, A. Senzanje, and A. Mhizha, "Estimation of small reservoir storage capacities in Limpopo River Basin using geographical information systems (GIS) and remotely sensed surface areas: Case of Mzingwane catchment," *Phys. Chem. Earth Pt. A/B/C*, vol. 31, no. 1516, pp. 935 – 943, 2006.
- [36] D. Amitrano, G. Di Martino, A. Iodice, D. Riccio, and G. Ruello, "Small Reservoirs Extraction in Semi-Arid Regions Using Multitemporal Synthetic Aperture Radar Images," *IEEE J. Sel. Topics Appl. Earth Observ.*, vol. 10, no. 8, pp. 3482–3492, 2017.
- [37] D. Amitrano, F. Ciervo, G. Di Martino, M. N. Papa, A. Iodice, Y. Koussoubé, F. Mitidieri, D. Riccio, and G. Ruello, "Modeling Watershed Response in Semiarid Regions with High Resolution Synthetic Aperture Radars," *IEEE J. Sel. Topics Appl. Earth Observ.*, vol. 7, no. 7, pp. 2732–2745, 2014.
- [38] ESA (European Space Agency), "The TIGER Initiative 2009-2012 Report," ESA, Tech. Rep., 2012.
- [39] E. P. Cox, "A method of assigning numerical and percentage values to the degree of roundness," *J. Paleontol.*, vol. 1, no. 3, pp. 179–183, 1927.
- [40] D. Amitrano, G. Di Martino, A. Iodice, D. Riccio, and G. Ruello, "An end-user-oriented framework for the classification of multitemporal SAR images," *Int. J. Remote Sens.*, vol. 37, no. 1, pp. 248–261, 2016.
- [41] L. Shapiro and G. Stockman, *Computer Vision*. Upper Saddle River, NJ: Prentice Hall, 2002.
- [42] J. Marr and E. Hildreth, "Theory of edge detection," *Proceedings of the Royal Society B*, vol. 207, no. 1167, pp. 187–217, 1980.
- [43] O. J. Tobias and R. Seara, "Image segmentation by histogram thresholding using fuzzy sets," *IEEE Trans. Image Process.*, vol. 11, no. 12, pp. 1457–1465, 2002.
- [44] D. Amitrano, V. Belfiore, F. Cecinati, G. Di Martino, A. Iodice, P.-P. Mathieu, S. Medagli, D. Poreh, D. Riccio, and G. Ruello, "Urban Areas Enhancement in Multitemporal SAR RGB Images Using Adaptive Coherence Window and Texture Information," *IEEE J. Sel. Topics Appl. Earth Observ.*, vol. 9, no. 8, pp. 3740–3752, 2016.
- [45] J. B. Campbell and R. H. Wynne, *Introduction to Remote Sensing*. New York, NY 10012: The Guilford Press, 2011.
- [46] J. Sanjal and X. X. Lu, "Application of remote sensing in flood management with special reference to Monsoon Asia: A Review," *Natural Hazards*, vol. 33, pp. 283–301, 2003.
- [47] D. Amitrano, G. Di Martino, A. Iodice, F. Mitidieri, M. N. Papa, D. Riccio, and G. Ruello, "Sentinel-1 for Monitoring Reservoirs: A Performance Analysis," *Remote Sens.*, vol. 6, pp. 10676–10693, 2014.
- [48] R. L. Thorndike, "Who belongs in the family?" *Psychometrika*, vol. 18, no. 4, p. 267276, 1953.
- [49] C. A. Sugar and G. M. James, "Finding the number of clusters in a dataset," *Journal of the American Statistical Association*, vol. 98, no. 463, pp. 750–763, 2003.
- [50] R. Lleti, M. Ortiz, L. Sarabia, and M. Snchez, "Selecting variables for k-means cluster analysis by using a genetic algorithm that optimises the silhouettes," *Analytica Chimica Acta*, vol. 515, no. 1, pp. 87 – 100, 2004.
- [51] U. C. Benz, P. Hofmann, G. Willhauck, I. Lingenfelder, and M. Heynen, "Multi-resolution, object-oriented fuzzy analysis of remote sensing data for GIS-ready information," *ISPRS J. Photogrammetry Remote Sens.*, vol. 58, pp. 239–258, 2004.